

Electron signals in the Forward Calorimeter prototype for ATLAS

J.C. Armitage,^a A. Artamonov,^b L. Babukhadia,^{c4} M. Dixit,^a T. M. Embry,^{c1}
V. Epshteyn,^b P. Estabrooks,^{a5} P. Gravelle,^a J. Hamm,^{c4} V. Khovansky,^b
D. A. Koolbeck,^{c4} P. Krieger,^{a2} P. Loch,^{c*} M. Losty,^{a3} J. Mayer,^{d4} R. Mazini,^{e2}
F. Gerald Oakham,^a M. O'Neill,^{a4} R.S. Orr,^d J.P. Rutherford,^c M. Ryabinin,^b
A. Savine,^c C. Jason Seely,^{c4} P. Shatalov,^b L.S. Shaver,^{c5} M.A. Shupe,^c G. Stairs,^{d4}
D. Tompkins,^c W. Trischuk,^d K. Vincent^{d4} and V. Zaitsev^b

^aPhysics Department, Carleton University, Ottawa, Ontario K1S 5B6, Canada

^bITEP Moscow, 117 259 Moscow, Russia

^cPhysics Department, University of Arizona, Tucson, Arizona 85721, U.S.A.

^dPhysics Department, University of Toronto, Toronto, Ontario M5S 1A7, Canada

^eUniversité de Montréal, Montréal, Quebec H3C 3J7, Canada

¹now at the Graduate College, University of Arizona, Tucson, Arizona 85721, U.S.A.

²now at the Physics Department, University of Toronto, Toronto, Ontario M5S 1A7, Canada

³now at TRIUMF, Vancouver, British Columbia V6T 2A3, Canada

⁴now in private sector

⁵retired

E-mail: loch@physics.arizona.edu

ABSTRACT: A pre-production prototype of the Forward Calorimeter (FCal) for the ATLAS detector presently under construction at the Large Hadron Collider (LHC) at CERN, Geneva, Switzerland, was exposed to electrons in the momentum range from 20 to 200 GeV/c in a test beam experiment at CERN in 1998. The measured performance, including a signal linearity within about $\pm 1\%$ and a high energy limit in the relative energy resolution of about 4%, meets the expectations for this kind of calorimeter, and exceeds the physics requirements for successful application in ATLAS.

KEYWORDS: Cryogenic detectors, Liquid detectors, Calorimeters.

*Corresponding author.

Contents

1. Introduction	2
2. The FCal pre-production prototypes in the test beam	4
2.1 Module mechanics	4
2.2 Signal formation	5
2.3 The prototypes in the test beam cryostat	7
2.4 Calorimeter readout electronics	8
2.5 The beam line	9
2.6 Triggering and data acquisition	9
3. Event selection	10
3.1 Particle tracking	11
3.2 Electron definition with calorimetric variables	12
4. Electron simulations	14
4.1 Geometry setup in the simulation	14
4.2 Particle generation	14
4.3 Signal reconstruction	14
5. Electron signals in FCal1	16
5.1 Signal linearity	16
5.2 FCal1 electron energy resolution	18
5.3 Cylindrical clustering	20
5.4 Further optimization of the energy resolution	22
5.5 Impact point reconstruction	22
6. The electron response in FCal2	25
6.1 Electron signal linearity in FCal2	26
6.2 Signal impact point dependence	26
7. Conclusions and outlook	27
A. Module geometry details	28

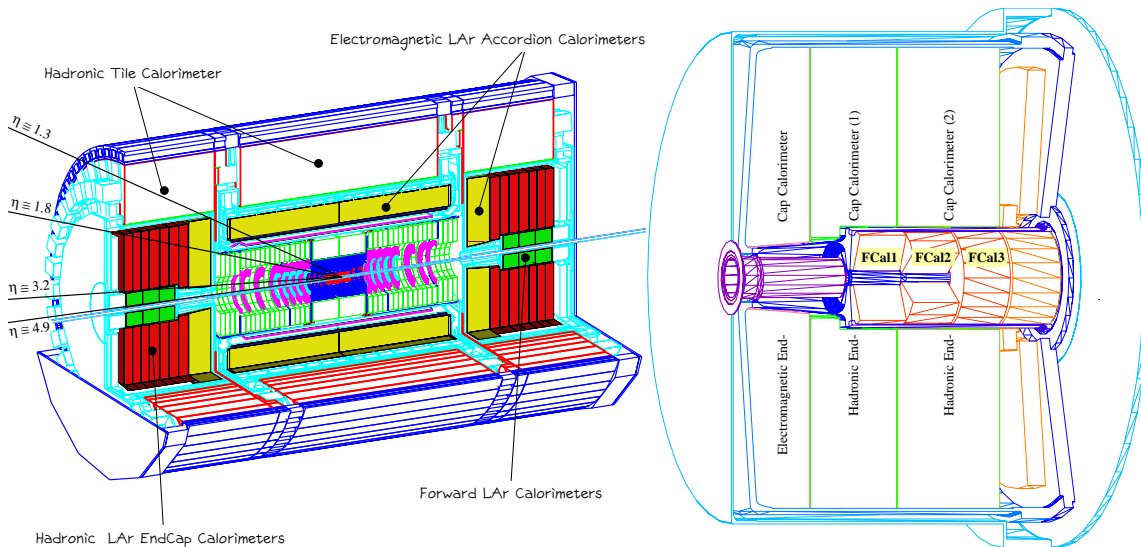


Figure 1. The ATLAS calorimeter system (left) and the three modules of the integrated Forward Calorimeter (FCal1/2/3) in the end-cap cryostat (right).

1. Introduction

The ATLAS detector at the future Large Hadron Collider (LHC) at CERN, Geneva, Switzerland, has calorimetric coverage up to pseudo-rapidities of about $|\eta| < 4.9$ [1–3], see figure 1. The most forward coverage $3.2 < |\eta| < 4.9$ is provided by the Forward Calorimeter (FCal). This calorimeter not only features a highly integrated design (figure 1), but also a novel readout electrode geometry well adapted to the challenging energy reconstruction and particle detection in this complex region of the ATLAS detector.

The most important physics requirements for the reconstruction of particles in the forward direction in LHC collisions come from the possible significant improvement of the missing transverse energy reconstruction through increased coverage in η , and a certain sensitivity to forward going jets, as in vector boson fusion events (longitudinal WW scattering). It is interesting to note that the actual energy resolution requirement for particle jets in the forward direction is [1]:

$$\frac{\sigma_E}{E} = \frac{100\% \sqrt{\text{GeV}}}{\sqrt{E}} \oplus 10\% . \quad (1.1)$$

Even this relatively modest requirement can already be challenging to meet at LHC, due to the typically complex signal environment introduced by the high energy and high rate particle flux in the pp collisions at $\sqrt{s} = 14$ TeV in this region, especially at the design luminosity of $10^{34} \text{ cm}^{-2} \text{ s}^{-1}$ and with bunch crossing intervals of only 25 ns. This environment severely limits the detector choices and thus the efficiency for the detection of forward-going electrons and photons as well as the achievable precision of the energy and direction measurements for these particles. The most important upper limit for relative signal fluctuations for electrons and photons under these conditions is actually implicitly contained in eq. (1.1) and can be estimated by $\sigma_E/E \lesssim 35\% \sqrt{\text{GeV}}/\sqrt{E} \oplus 5\%$.

Signal linearity for electrons and photons is required within $\pm 2\%$, again motivated by the jet response requirements in this region. Finally, it is possible to estimate the angular resolution

requirements for electrons and photons in the FCal using a constraint on the transverse energy resolution σ_{E_T}/E_T . For example, $\sigma_\eta < 0.05$ is needed to achieve the required $\sigma_{E_T}/E_T < 7\%$ limit for $E_T > 50$ GeV at $|\eta| = 3.7$ in the ATLAS FCal.

As already indicated above, the forward direction at LHC is characterized by high radiation levels induced by the large flux of high energetic particles scattered in this region. The design of the ATLAS FCal accommodates this environment with respect to signal stability, i.e. no significant signal gain changes in the active medium due to changing radiation levels following the (normal) drop of the instantaneous luminosity in the course of a data run. In addition, the FCal is expected to provide general long term operational survivability for at least 15 years of LHC running at design luminosity, without mechanical (general disintegration of detector components) or electrical (loss of high voltage, disintegration of signal cables) degradation of the detector in this environment.

The electromagnetic Forward Calorimeter (FCal1) is a copper/liquid argon calorimeter, featuring thin annular argon gaps. The hadronic modules FCal2 and FCal3 have the same general electrode geometry, with tungsten as the primary absorber material. The thin gap electrodes avoid positive argon ion build-up in the radiation environment [4], and are thus expected to provide stable signals independent of the radiation level, with only insignificant gain variations at a fixed direction.¹ The material choices for the absorber were motivated by considerations concerning general radiation hardness and limited activation during the lifetime of LHC, while maintaining the physics performance requirements as discussed above, and providing a high density detector to assure as much as possible complete absorption even at highest particle energies (several TeV possible) in addition to the limited lateral shower sizes favoured for particle and jet reconstruction in the radiation environment. See [3, 5] for more detailed descriptions of these calorimeters and their performances.

Several prototypes for the electromagnetic module were successfully tested in particle beams at Brookhaven National Laboratory and CERN [6–8]. Quarter segment, full depth pre-production prototypes for FCal1 and FCal2 (so-called "Module 0s") were designed and built in Arizona and Canada, respectively, in 1998, and submitted to an extensive test beam program with electrons, pions and muons at CERN the same year. These modules had the same signal characteristics as the final production modules, thus allowing a very realistic performance evaluation for the FCal electron response in ATLAS.

In this article we present results for electron signals in the FCal1 and FCal2 modules, respectively. We start with a description of these special modules in section 2, including an outline of the test beam setup from relevant beam-line details to readout electronics. Event selection is a very important step in the analysis and is discussed in section 3. This is followed by a description of the GEANT3.21 [9] and GEANT4.0.2 [10] setup used to simulate the electron response, in section 4. Results for important electromagnetic performance parameters such as signal linearity, energy and spatial resolution in FCal1 are presented in section 5, together with selected comparisons to simulations. The electron response of the hadronic FCal2 module is briefly discussed in section 6. Conclusions and outlook can be found in the last section 7.

¹There is a direction dependent loss of gain due to the incoming particle flux and energies increasing with η . The corresponding increasing ionization levels induce increased currents in the liquid argon gap which cause the electric field to drop, leading to systematic signal gain reductions up to 12% at the highest $|\eta| \approx 4.9$. This loss can be corrected using the actual current draw measured on the high voltage lines, for example.

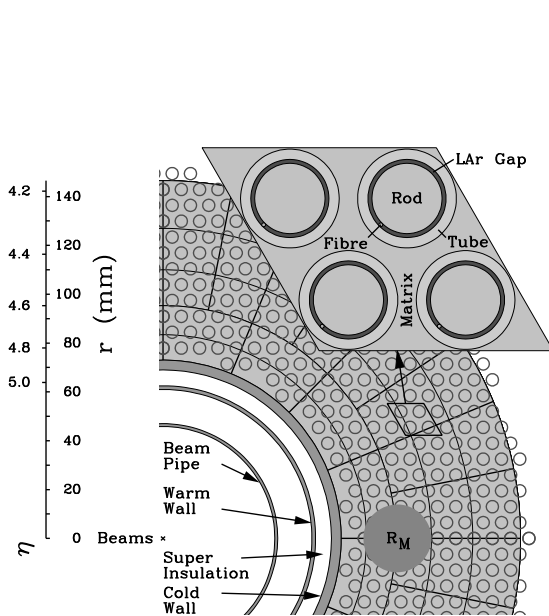


Figure 2. The hexagonal electrode pattern in the FCal1 absorber matrix. The Moliere Radius R_M is indicated in addition.

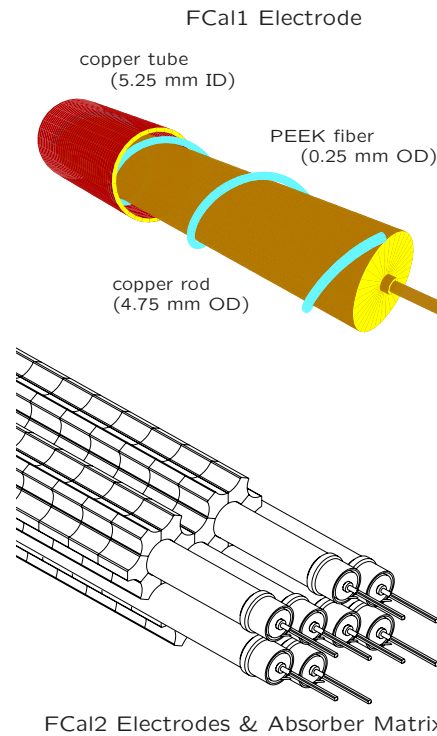


Figure 3. One of the FCal1 tubular electrodes (top). The shape of the tungsten slugs packing the interstitial space between electrodes in FCal2 is shown at the bottom.

2. The FCal pre-production prototypes in the test beam

This section contains a description of the mechanics and the readout organization of the FCal1 and FCal2 test beam modules. Most of the features described here are similar for the final detector, with some minor differences in the readout structure at the inner and outer edge of the larger production modules. In addition, we discuss relevant details of the test beam setup, including the data acquisition and trigger elements.

2.1 Module mechanics

The FCal pre-production prototypes were full depth quarter segments of the actual cylindrical modules, with $3/16(1/4)$ of the volume of the full FCal1(2) instrumented. Both modules featured the tubular electrodes formed by thin wall copper tubes and copper (FCal1) or tungsten (FCal2) rods. The argon gap sizes were about $260 \mu\text{m}$ in FCal1 and $375 \mu\text{m}$ for FCal2, with electrode center-to-center distances of about 7.5 and 8.2 mm, respectively, see figure 2. The argon gaps were maintained by nylon fiber of appropriate diameter wound around the FCal1 rods (figure 3), and three PEEK spacers clipped onto the FCal2 rods. This is a departure from the design of the final production modules, where all spacers are wound PEEK fibers. Contrary to nylon fibers, the PEEK fibers provide the necessary radiation hardness for operations in the forward region in ATLAS,

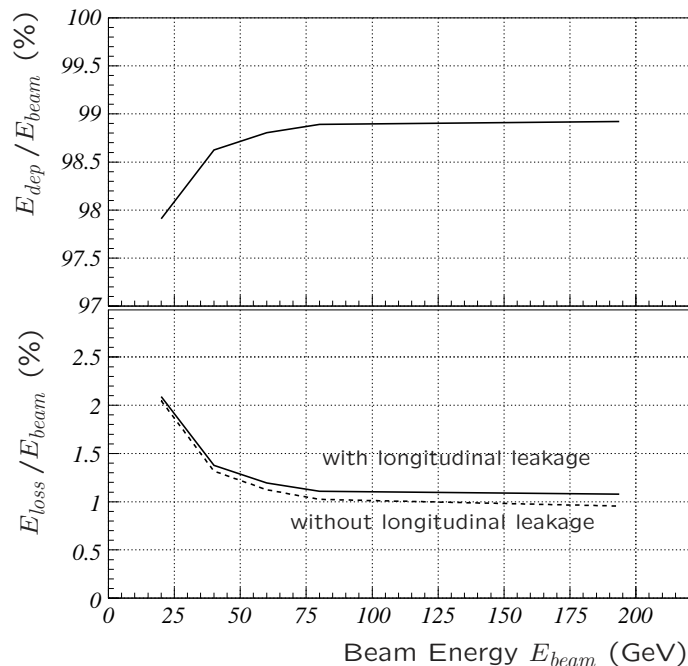


Figure 4. Integrated shower containment for electrons in FCal1, calculated by the ratio of average deposited (E_{dep}) over beam energy (E_{beam}) in GEANT4 simulations, as function of E_{beam} (upper plot). The relative energy losses, calculated by the ratio of the leaked energy $E_{loss} = E_{beam} - E_{dep}$ to E_{beam} , including (solid line) and excluding (dashed line) longitudinal losses, again as function of E_{beam} , is shown in the lower plot.

which is characterized by significant residual radiation activity. They also have fewer mechanical problems than the clips in the insertion process, for example. The signal characteristics, on the other hand, are not affected by the different spacer designs.

The FCal1 absorber can, in many respects, be viewed as a monolithic copper wedge with holes for the electrode assemblies. The outer radius of the wedge was 45 cm, and the overall module depth was also 45 cm. This depth corresponds to approximately 28 radiation lengths (X_0). In addition, a sufficient lateral extension around the beam impact area allowed nearly complete absorption of electromagnetic showers, as confirmed with electron shower simulations, see figure 4. Nearly all of the energy losses occurred in materials upstream of the calorimeter. The beam spot itself is illustrated in figure 5.

The FCal2 absorber consisted of approximately 180000 small tungsten slugs filling the space between the electrode tubes, see figure 3. The slugs were held in place by these tubes, copper front- and end-plates, and copper form pieces on the sides of the module. The much denser absorber made this module much deeper for electrons, with about 91 X_0 in total. More construction details can be found in appendix A, including a summary of the principal mechanical, electrical, and calorimetric parameters of the FCal1 and FCal2 modules in table 3.

2.2 Signal formation

Signals from individual electrodes were read out through two summing stages. First, small interconnect boards collected signals from groups of four and six electrodes on the front face of

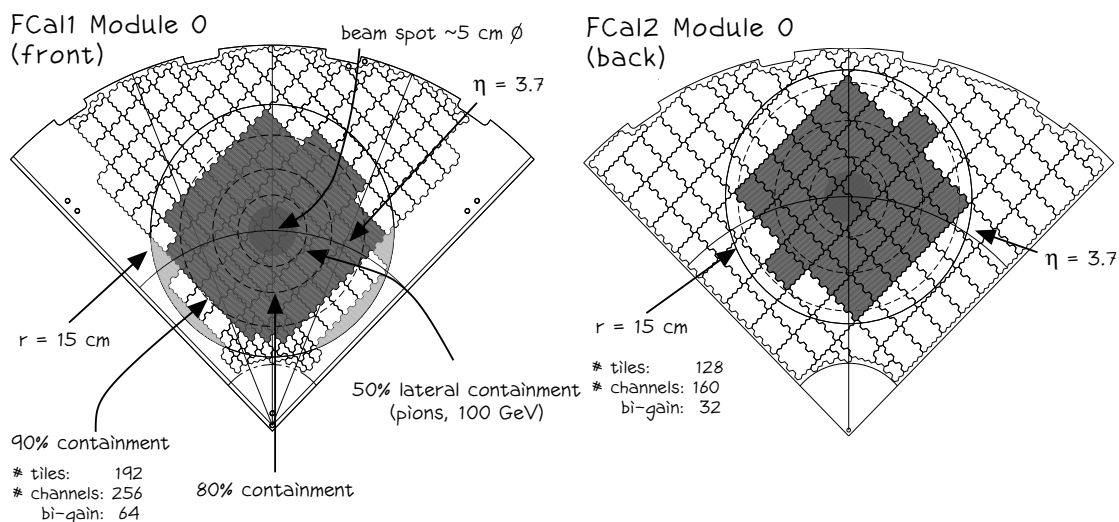


Figure 5. Tiled readout cell contours on the FCal1 prototype module front face (left) and the FCal2 prototype module rear face (right). The dark shaded circles indicate the size of the beam spot in the test beam ($r = 2.5$ cm), while the light shaded areas indicate cells with bi-gain readout. The curved line shows the impact pseudo-rapidity $\eta = 3.7$ in ATLAS.

FCal1 and the back face of FCal2, respectively. The signals from these electrode groups were then summed by fours again, except for the electrodes closest to the beam pipe in ATLAS, and some small groups at the outer perimeter of the modules. In these special locations the initial electrode groups were read out directly. This kind of summing introduced a pattern of small (four or six electrodes) and large (16 or 24 electrodes) calorimeter cells, each independently read out. The total number of cells in the FCal1(FCal2) prototype was 192(128), see figure 5.

The final stage summing was performed by auto-transformers, which combined the four inputs into one output such that each input signal saw the same impedance. This avoided signal losses and actually allowed signal summing with slightly less noise contribution than regular wire connections. The transformers were installed on summing boards, each of which mapped 4×64 inputs from the electrode groups onto one 64 channel output. The cables running from the module interconnect boards to the summing boards were about 3.5 m long. The cables were Kapton²-wrapped coaxials with a nominal impedance of 25 Ω .

The summing boards also handled the high voltage (HV) distribution providing the electric field of approximately 1 kV/mm in the electrodes (250 V for FCal1 and 375 V for FCal2). There were four independent HV lines on each summing board, each assigned to one of the input connectors. The HV was distributed to the individual electrode groups through a 1 M Ω protection resistor, and decoupled from the signal by a 12 nF capacitor, see figure 6.

A total of five summing boards were located inside the liquid argon volume, close to the calorimeter modules. Three of the boards were used to form the 192 cell signals from the FCal1 prototype module. The 128 cell signals from the FCal2 module were formed on the remaining two boards.

²Registered trademark of E.I. du Pont de Nemours & Co. (DuPont).

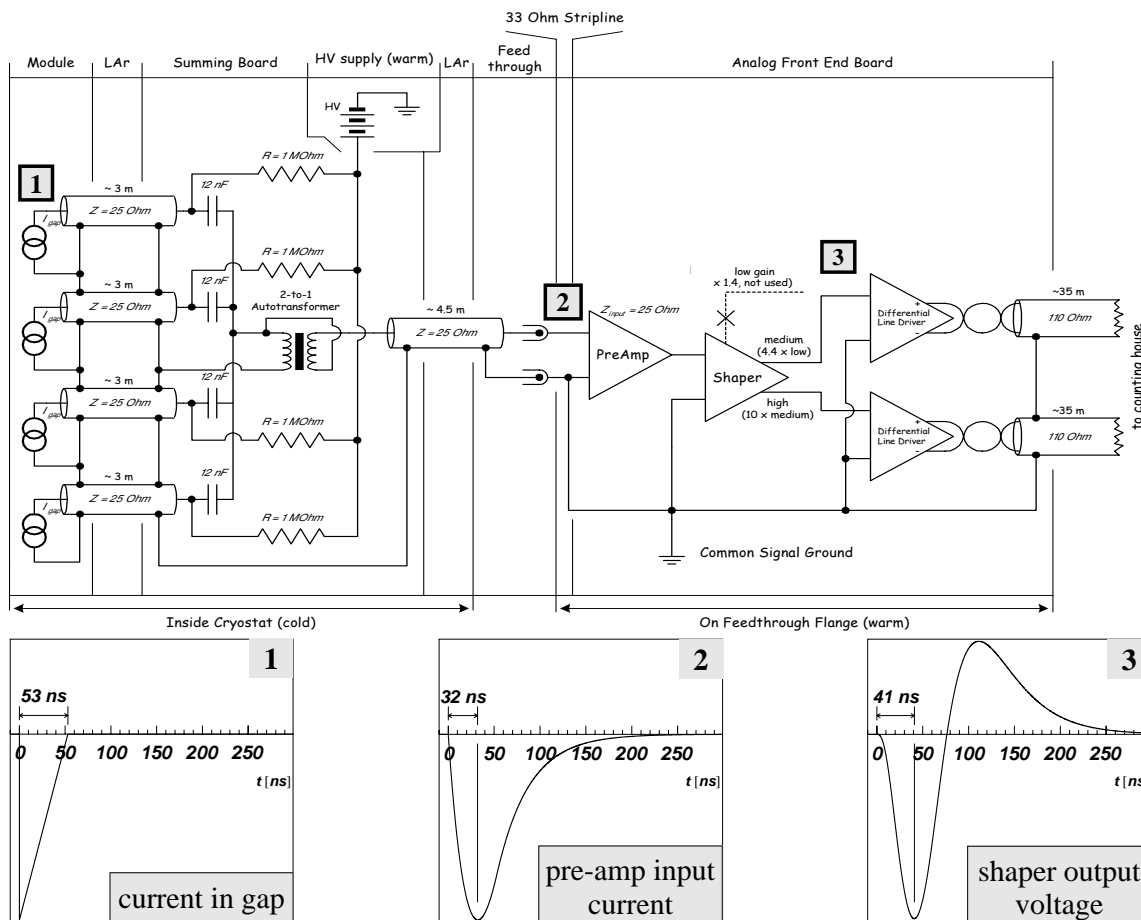


Figure 6. Electronic model of the FCal pre-prototype readout. The current sources on the left indicate a group of four or six tubular electrodes in FCal1 and FCal2, respectively. The evolution of the signal shape is shown at the bottom.

2.3 The prototypes in the test beam cryostat

The 1998 test beam consisted of two separate run periods. The first was with the FCal2 prototype in a standalone setup, and the second was with a combined FCal1/2 setup. In both cases the calorimeter modules were mounted into a large cryostat at the end of CERN’s H6 beam line. A schematic view of the beam line is shown in figure 7.

In the FCal2 standalone program this module was directly exposed to the beam particles, i.e. it was located closest to a thin window in the cryostat, thus minimizing the amount of inactive material in front of it. As was also the case for the common FCal1/2 setup, the FCal2 prototype was tilted by about 2.7° with respect to the beam axis.

For the combined setup, the electromagnetic FCal1 module was located in front of the hadronic FCal2 module, similar to the configuration in ATLAS. Upstream of FCal1, but still inside the cryostat, was a piece of low density liquid argon excluder (Rohacell³), to reduce the amount of inactive material in front of this calorimeter. Another piece of excluder was mounted directly behind the FCal2 module, thereby reducing the amount of material between the FCals and the warm tail-catcher calorimeter, see figure 7.

³Registered trademark of Degussa GmbH

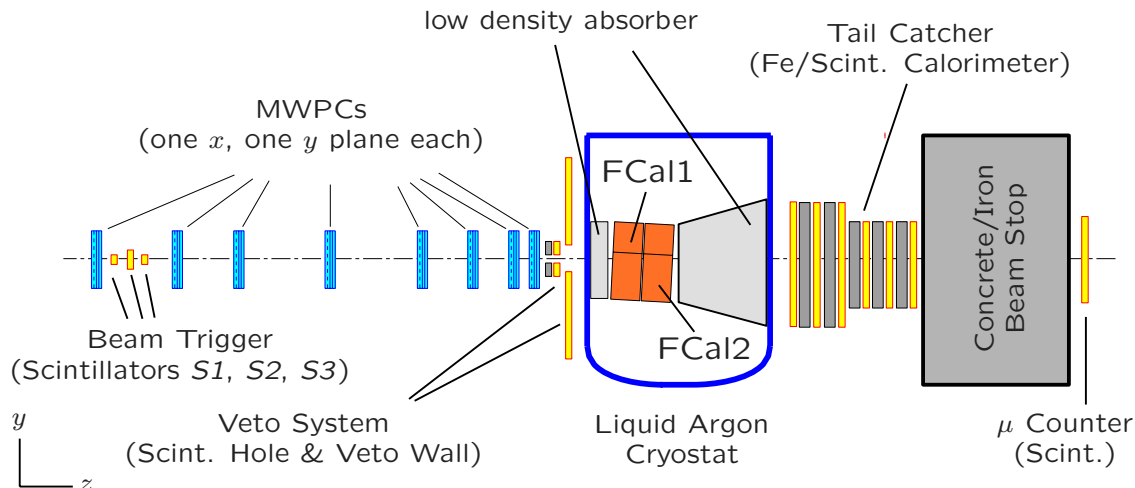


Figure 7. Schematic view of the beam line instrumentation for the ATLAS FCal pre-production prototype test beam (not to scale). The particle beam enters from the left of the drawing.

Both modules were tilted around the horizontal axis by 2.7° . The nominal impact position in the center of the module then corresponds to a pseudo-rapidity $\eta \approx 3.7$ in ATLAS. This was also the direction of the largest depth of the combined FCal prototype system.

2.4 Calorimeter readout electronics

The signal readout for the FCal pre-production prototypes featured a very similar signal treatment as in the final detector, especially with respect to the signal routing, and the analog signal amplification and shaping. The main difference was in the digitization, where for this experiment the signal amplitude was directly converted, while in ATLAS the signal shape is sampled in time, and the amplitude is reconstructed online from these signal samples.

The signals from the cold summing boards described above were fed to the warm analog electronics through about 4.5 m long cable harnesses in the cold, a feed-through flange transferring the signals from the cold to the warm side, and a baseplane distributing the analog signals to the pre-amplifiers and shapers on the analog Front End Board (FEB).

The typical impedance of the whole transfer line was 25Ω , thus matching the input impedance of the pre-amplifiers. Figure 6 shows an electronic model of the analog FCal readout chain.

The FEB was a prototype design handling 128 inputs. Each of these inputs was connected to a pre-amplifier/shaper unit, which were packaged by fours (32 chips in total). The pre-amplifiers and shapers were close to the standard ATLAS design [13–15]. For example, the shaper had three gain stages on the output, with the following approximate amplification levels with respect to the pre-amplifier output:⁴ low ($\times 1.4$), medium ($\times 6.2$), and high gain ($\times 62$). Due to the limitations in available energies, the lowest gain was not needed in the test beam experiment, thus only the high and medium gain stage were read out. With this special configuration, the 11-bit readout

⁴The ratio between low, medium and high gains in the FCal readout in ATLAS is actually close to 1 : 10 : 10, with an effective dynamic range of about 16 bits, covering the full range from about 80(160) MeV to approximately 5(10) TeV in a single FCal1(FCal2) channel.

granularity in this experiment was extended to nearly 14 bits dynamic range between approximately 20(40) MeV and 300(600) GeV, with a typical electronic noise of about 250(500) MeV in a single FCal1(FCal2) channel.

The standard readout for all FCal1 and FCal2 channels was the high gain signal. To accommodate higher energies in individual cells, 64 cells around the beam spot in FCal1 and 32 cells around the beam spot in FCal2 (see figure 5) were read out with an additional medium gain stage. This avoided saturation of cell signals, which in high gain typically occurred at 30 GeV electron energy in FCal1, and at 60 GeV electron energy in FCal2. The ratio between the gain stages was close to 10, thus allowing the medium gain to safely accommodate the highest possible electron beam energy of 200 GeV in one cell.

The shaped signals were picked up by differential line drivers on the front end boards and transmitted on about 35 m long shielded twisted pair cables to the digitization and recording units in the counting house, see figure 6. Any direct wire connection between the modules was avoided for both signal and ground, to minimize electronic noise pick-up, especially through ground loops.

2.5 The beam line

The H6 beam in CERN's North Area is a secondary particle beam provided by the SPS, which delivers electrons, pions and muons with momenta from typically 10 to 200 GeV/c. The schematic depiction in figure 7 shows the instrumentation of the FCal module test beam line, starting directly after the last bending magnet, and including the various detectors used for online triggering and offline event selection, the cryostat with calorimeter modules, the tail-catcher and beam stop, and the final muon scintillator counter.

The overall beam line instrumentation covered approximately 35 m of particle passage through air. The most upstream scintillator counters *S1*, *S2*, and *S3*, shown on the far left in figure 7, provided the fast particle trigger signal. Individual particle tracks were reconstructed from signals from a set of eight multi-wire proportional chambers (MWPCs). These were distributed along the flight path of the particles, starting close to the last bending magnet and going up to a few meters in front of the cryostat. Five of the MWPCs had a vertical and horizontal wire plane, while the remaining three chambers featured one plane only, either horizontal or vertical. The typical space point resolution was on the order of 0.5 mm.

The veto system consisted of a hole counter and a veto wall. The hole counter detected particles outside a 5 cm diameter circular area around the central beam axis, while the scintillators in the veto wall detected particles scattered at larger angles from the beam axis.

The tail-catcher was a coarse iron/scintillator calorimeter located directly behind the cryostat containing the FCal detectors. Beyond the tail-catcher was a concrete beam stop followed by a single muon counter to record particles passing through this beam stop.

2.6 Triggering and data acquisition

The main event trigger was a low bias particle trigger, generated by each beam particle producing a signal amplitude corresponding to the crossing of at least one minimum ionizing particle in each of the three upstream scintillators *S1*, *S2*, and *S3*, see figure 7 (triple coincidence requirement). No other signal from the beam instrumentation was used for event selection in the (fast) trigger,

especially no active veto. The signals from the veto counters, the tail catcher calorimeter, the muon scintillator, and some logical combinations of beam counter signals indicating possible event pile-up, were latched into a trigger word, which could then be used for fast event selection in the online monitoring and/or offline event reconstruction. The data taking rate was solely determined by the incoming particle flux (set by collimators in the beam) and the very short dead time of the acquisition system.

Monitor and random triggers were also initiated during the SPS particle burst in H6, each at a rate of typically 5% of all triggers. The corresponding events helped to monitor the whole system during actual data taking, especially with respect to electronic gain stability, pedestal drifts in the analog-to-digital converters (ADCs), and electronic noise.

The data acquisition (DAQ) for the 1998 test beam was very similar to the one used in the earlier FCal test beam efforts [8], and reflects a significant departure from the ATLAS calorimeter readout in that only the signal amplitude is recorded, not the signal shape in time. In this test beam setup the signals on the warm cables were received by track & hold amplifiers, which were gated by the event trigger. The timing of the hold gate pulse had to be adjusted to the peaking time of the FCal pulse, and it had to be stable within ± 2 ns, for which the FCal pulse around its peak changed by 0.5% at most. The signals from the trigger counters $S1$, $S2$, and $S3$ were timed as well as the calorimeter signal itself. The major source of timing fluctuation for the hold gate pulse was the reference (start) signal from $S1$, which contributed about $\sigma_t(S_1) \approx 320$ ps to the total trigger time jitter of about $\sigma_t \approx 350$ ps. This means that there was no significant contribution of readout timing instabilities to fluctuations of the FCal signal.

The held signal amplitude was converted channel-by-channel by 11 bit ADCs. These calorimeter ADCs, as well as all other ADCs for beam line detectors, time-to-digital converters and shift registers for the MWPCs, input registers for the trigger word, and scalers for event timing, were read out through CAMAC into a personal computer during the SPS particle spill (approximately 2 s) and finally stored on a disk during the break between two spills (approximately 16 s). The typical event rate was 800 events per spill, i.e. about 400 Hz. In total, approximately 35 million events were recorded in about 35 Gbytes for both run periods.

3. Event selection

One of the consequences of the ATLAS Forward Calorimeter design is the inhomogeneous front face. Depending on its impact position, the incoming particle may traverse a significant amount of relatively soft liquid argon before hitting the absorber, or hit the absorber first and start developing its shower earlier. Even though there is no tunneling of particles in the liquid argon gap, even at the relatively small impact angles with respect to the electrode orientation [8], a relevant signal variation in the order of 10% for FCal1 was observed and methods were developed to correct for this effect using calorimeter information only, see [6, 16, 17] and later in this note (section 5.5).

High statistics with clean electron events and uniform illumination of a calorimeter region of at least the size of the lateral electrode dimensions with particles was mandatory to determine the average signal behavior, and to ensure sufficient precision to develop and test impact point determination and signal correction methods. We therefore used beam optics which provided wide open, de-focused beams close to the calorimeter front face with a beam profile typically flat within

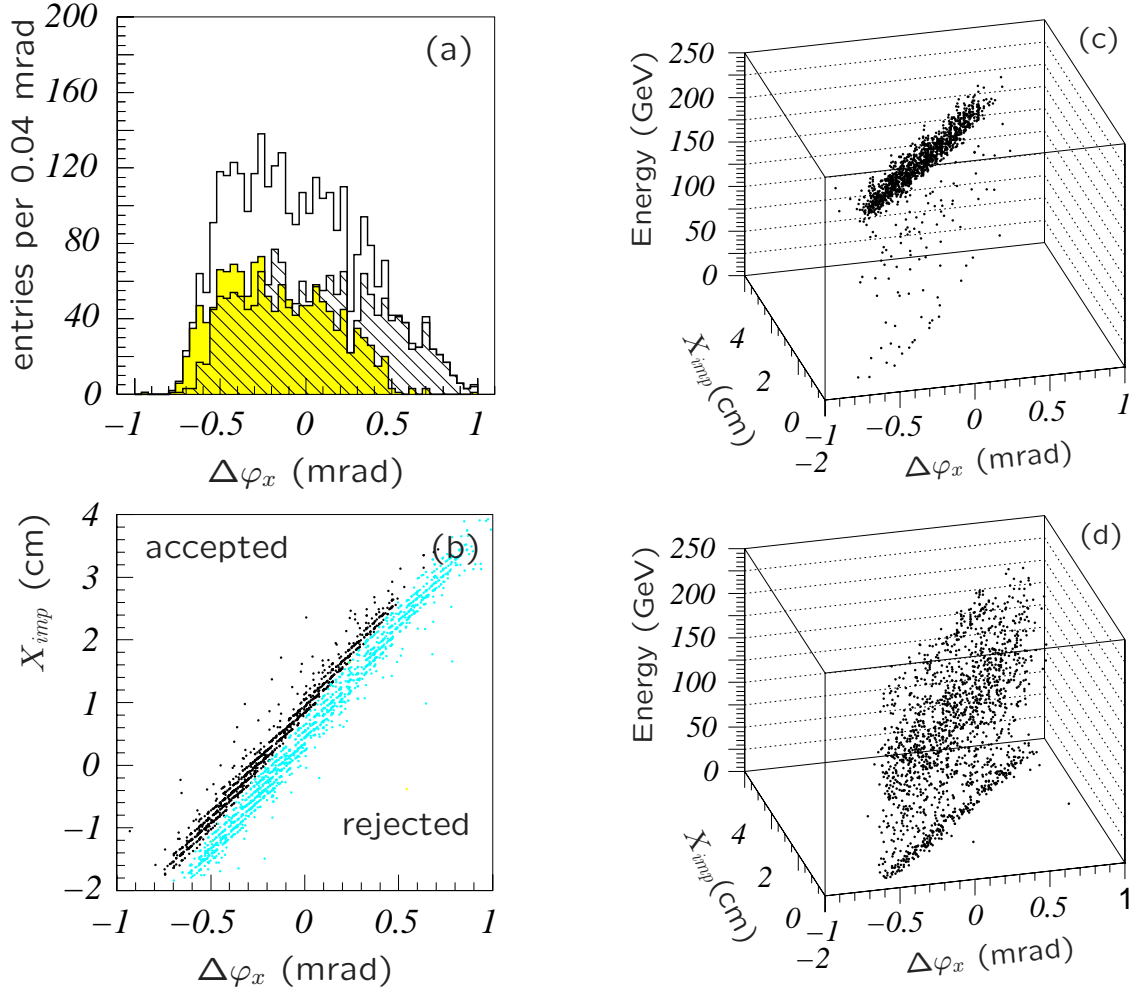


Figure 8. Distribution of the horizontal angular beam deflection $\Delta\phi_x$ (a), for accepted events (shaded), rejected events (hashed) and all events (solid line). The correlation between the horizontal impact point coordinate X_{imp} and $\Delta\phi_x$ shows a two-band structure, with the events accepted as electrons at this stage indicated by black dots (b). The reconstructed energy in FCal1 versus X_{imp} and $\Delta\phi_x$ is shown in (c) for accepted events, and in (d) for rejected events (all for a nominal 200 GeV/c beam).

a circle with radius $r = 2.5$ cm. The system of MWPCs provided track and vertex information on an event-by-event basis.

The H6 facility delivered a rather clean electron beam for momenta up to 80 GeV/c just by correct setting of the beam optics, secondary targets, and filters. Higher momentum beams typically had pion and muon contamination. Even though these particles were slightly separated in phase space, it was not always possible to sufficiently suppress them online by just using elements of the beam optics. Signals from the beam line and leakage detectors, and signals from the two FCal modules themselves, were used in addition for offline event selection.

3.1 Particle tracking

Particle-by-particle track information was not only very useful to determine the impact point with

relatively high precision (order 0.5 mm from the MWPCs), but also to separate pions and electrons at higher energies.

A particle track was defined by a straight line extrapolation using the space points from MWPC hits in the vertical and horizontal planes. Typically five space points per track were available. Events with more than one cluster in any of the chambers were rejected, as well as tracks measured with less than three space points or with low fit quality. A particle vertex in the vertical plane was determined by track extrapolation to the rear face of the last bending magnet, while the impact point was reconstructed by track extrapolation to a (virtual) vertical plane just in front of the calorimeter.

The beam envelope was defined by the horizontal and vertical angular deflection of the individual particle track from the nominal beam line, and the extrapolated horizontal and vertical impact point coordinates. The most discrimination power was achieved for the highest beam momentum (200 GeV/c) by combining the two variables in a given plane. Any separation between electrons and pions observed was mainly due to the energy loss of electrons due to bremsstrahlung, which lowered their actual momentum from the nominal 200 GeV/c to effectively 193.1 GeV/c.

Figure 8 shows the effectiveness of the particle selection by phase space for a nominal 200 GeV/c beam. The spectra of the horizontal angular deflection $\Delta\phi_x$ in figure 8(a) confirm that $\Delta\phi_x$ alone has very little discrimination power. Only the correlation with the horizontal impact point coordinate X_{imp} allows the separation of electrons and pions in the beam: the particles in the lower band of $(\Delta\phi_x, X_{imp})$ in figure 8(b) more often produce smaller signals well below the beam energy E_{beam} , see figure 8(d), as expected for pion signals in FCal1. The particles in the upper band, on the other hand, often have their energy reconstructed in FCal1 close to E_{beam} , thus behaving much more like fully absorbed electrons (figure 8(c)).

3.2 Electron definition with calorimetric variables

The selection strategies and cuts discussed so far made exclusive use of secondary detectors in the beam line, mainly the MWPCs, with some limited efficiency, for example see figure 9(e). Additional improvement of the electron sample could be achieved by event selections based on reconstructed calorimeter variables. Care must be taken in the choice of calorimeter variables to minimize a possible introduction of biases in the electron event sample. The two signal features used here were sensitive to the electromagnetic shower development. The nearly complete longitudinal containment of electrons in FCal1, measured by the signal ratio F_{em} , and the general compactness of the electromagnetic showers in the copper absorber of this module, as measured by F_{max} , were defined as

$$F_{em} = \frac{E_1}{E_1 + E_2} \quad \text{and} \quad F_{max} = \frac{E_{1,max}}{E_1}. \quad (3.1)$$

Here E_1 and E_2 are the signals summed over all 192 cells in FCal1 and all 128 cells in FCal2, respectively, and $E_{1,max}$ is the signal in the FCal1 cell with the largest signal in the event.

F_{em} could be expected to be close to unity for electrons, but was subjected to fluctuations due to electronic noise, especially in FCal2, which generated two distinctively unphysical signal regions: $F_{em} < 0$ in completely noise dominated events (rejected), and $F_{em} > 1$ in events with negative signal in FCal2, which usually still were good electron candidates, see figure 9(a) and (c).

The shower compactness measured by F_{max} was typically high for electrons in FCal1, due to the fact that the cell size in this calorimeter is comparable with the Moliere Radius of the electro-

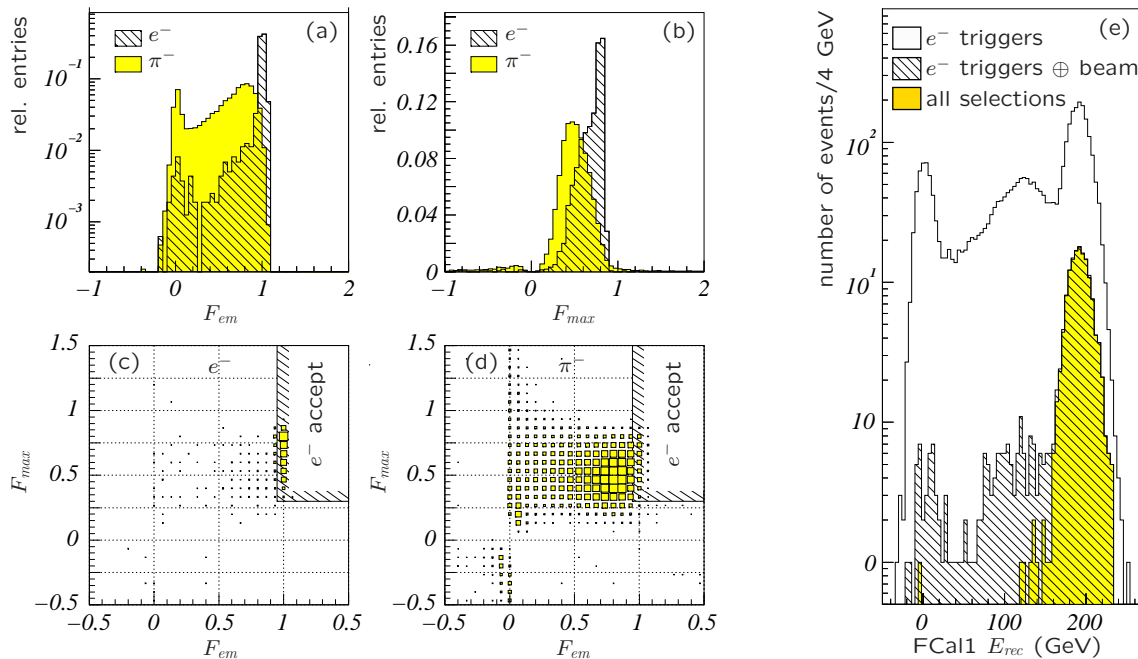


Figure 9. The distributions of the shower compactness variables F_{em} (a) and F_{max} (b), as defined in eq. (3.1), are shown together with the correlation between F_{em} and F_{max} , for 193.1 GeV/c electrons (c) and 200 GeV/c pions (d). The electron signal spectrum after all beam envelope cut and calorimetric event selections is shown in (e).

magnetic shower. As a consequence, often most of the electron energy was deposited in one or two cells only. Figure 9(b) and (d) show the distributions of these variables for pions and electrons. A combined selection of (F_{em}, F_{max}) , with the acceptance region indicated in figure 9(c) and (d), yielded the best discrimination power for electrons in FCal1, as can be seen in the cleaned-up spectrum in figure 9(e).

Up to 80 – 90% of the events at a given beam energy and configuration were dropped by principle data quality criteria,⁵ the calorimeter based selection, and, especially at the highest beam energy, the beam envelope cut. This assured well understood electron samples with minimal contamination by pions or protons ($< 10^{-5} - 10^{-6}$, depending on beam energy and charge). Due to the large number of events recorded to begin with, these high quality electron samples still contained several 10000 events available for analysis for FCal1 at each energy and beam configuration. The event numbers were less for the FCal2 standalone setup, with a bit more background due the fact that only the beam magnets, collimators, and additional targets and filters in the H6 beam line could be used to select electrons. This limited the available beam energies and rates. Here the typical statistics were samples of a few 1000 electrons for each analyzed energy.

⁵Includes principle vetoes from beam line counters, and the rejection of the small amount of events with irrecoverable technical problems like high voltage failures in any of the vital detectors, bit errors, and otherwise incomplete or suspicious readout.

4. Electron simulations

The determination of the performance parameters for electron detection and reconstruction in the FCal requires a good understanding of all important features of the experimental electron signal in this calorimeter. Detector signal simulations with both the GEANT3.21 package and the GEANT4.0.2 toolkit were used to understand the possible contributions to signal losses not directly accessible in the experiment, like the ones due to energy losses in upstream inactive materials, or possible lateral and longitudinal leakage and other inefficiencies of the test beam setup.

4.1 Geometry setup in the simulation

Specific care was taken to completely describe the geometry of the FCal modules and the beam line elements. The geometries in GEANT3 and GEANT4 were set up in as similar a fashion as possible⁶ in order to minimize systematic uncertainties in the comparison between the simulations and the test beam data.

All detectors discussed in sections 2.3 and 2.5 were implemented in the simulation, as were all other relevant inactive materials that may affect the signals in the various detectors and calorimeters, see figure 10.

The description of the FCal modules was as close as possible to the real detectors. For example, the electrode positions and the description of the summing stages, i.e. the signal collection into readout channels, were directly taken from the wiring database used in the module construction. The electrode geometry was taken from averages of sample measurements on the real hardware, whenever available. The actual composition of all materials was taken into account, again whenever possible.

Some simplifications had to be made, though, to allow for efficient simulation. Again as an example, the FCal2 bulk absorber is not described at the level of individual tungsten slugs, but rather as a mixture of slugs, the liquid argon which fills the (small) spaces around the slugs, and the copper tubes forming the cathodes.

4.2 Particle generation

The inhomogeneous front face of the FCal introduces a dependence of the signal on the impact point, as mentioned earlier. The shape of the total signal spectrum therefore depends on the horizontal and vertical beam profile, i.e. how many electrons in a given sample hit argon first, instead of the absorber material. To ensure an identical illumination in the simulations, we used the directions and vertices from particle tracks reconstructed in the experiment to generate particles in the simulation. This not only naturally generates the same beam profile, but also maintains the correlation between a given vertex and the track direction. The tracks and vertices used in the simulation were taken from the final experimental data sample used for the comparisons in this analysis. The simulated beam profile is therefore very similar to the experimental profile.

4.3 Signal reconstruction

The FCal signal in both the GEANT3 and GEANT4 simulations was the energy deposited in the liquid argon of the tube electrode (“visible energy”). It was collected into cells corresponding

⁶The two simulation packages use different methods to describe geometries.

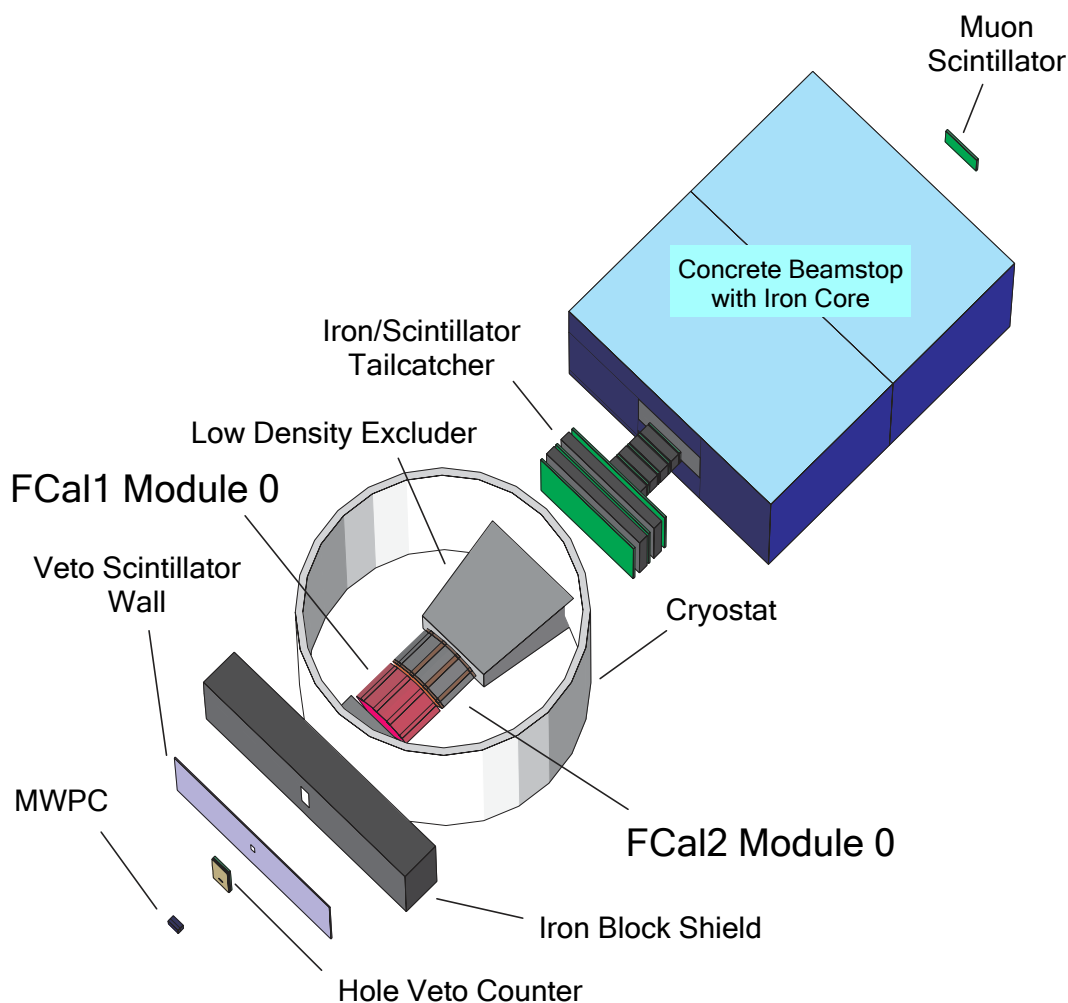


Figure 10. A part of the FCal pre-production prototype test beam setup in GEANT4. Relevant beam line detectors, the cryostat including the two FCal modules, the tail-catcher, the beam stop and the muon counter are shown. In this picture the particles enter the setup from the lower left corner.

to the ones in the experiment. Nevertheless, the signal in these cells was subjected to different inefficiencies in experiment and simulation, the most important ones being the thresholds for actual particle production in the simulation, and the electronic noise and digitization in the experiment.

The thresholds for particle tracking and explicit secondary particle production in the simulation are different in the two programs considered here. GEANT3 uses an energy threshold in both cases, while GEANT4 tracks particles to zero kinetic energy, but employs a minimum range requirement for production of secondaries in different materials. These cuts usually affect the simulated sampling fraction. To minimize possible simulation artifacts introduced on the signal, the lowest possible energy threshold of 10 keV was used in all materials in GEANT3. In case of GEANT4, only secondaries with prospective ranges of more than 0.5 mm were simulated.

The experimental signal in a given cell was affected by the characteristics of the analog electronics, especially the noise, and the digitization. Some of these experimental inefficiencies must

be included in the reconstruction of the simulation signal, to allow a detailed comparison of all relevant signal related variables. In particular the noise must be taken into account for comparisons of the relative energy resolution. This was done by adding the signals cell by cell from an experimental randomly triggered “empty” event to the simulated cell signal $E_{vis,i}$ in a simulated event:

$$E_{rec,i} = c_{MC} \cdot E_{vis,i} + E_{noise,i}, \quad (4.1)$$

where $E_{rec,i}$ is the energy reconstructed in a given cell i , c_{MC} the inverse electron sampling fraction in the simulation, and $E_{noise,i}$ the energy signal from the empty experimental event representing the electronic noise signal contribution. The randomly triggered empty event was taken inbetween particle triggers inside the spill, and the particular events used in the reconstruction of the simulated signals were taken from experimental data runs which were used in the comparisons in the final analysis. This assured that the experimental conditions affecting the noise at the time of the data taking were as much as possible included into the reconstruction of the simulated signals.

5. Electron signals in FCal1

The most important performance requirements for an electromagnetic calorimeter like FCal1 are the direct proportionality of the signal to the incoming energy (signal linearity), and an adequate energy resolution. Each of these parameters has been studied in quite some detail for the FCal1 pre-production module. The results are presented in this section, together with comparisons to GEANT3 and GEANT4 simulations.

5.1 Signal linearity

The experimental electron signal E_{rec} in the FCal1 module was reconstructed for all beam energies using the (experimental) calibration constant c_{exp} :

$$E_{rec} = c_{exp} \cdot A = c_{exp} \cdot \sum_{i=1}^{N_{cells}} a_i = \sum_{i=1}^{N_{cells}} E_{rec,i}, \quad (5.1)$$

with A being the sum of raw cell ADC signals a_i with pedestals subtracted, over all N_{cells} cells of FCal1. The calibration constant c_{exp} , in units of GeV/ADC count, was constrained by the ratio of the beam energy E_{beam} to the average response for electrons with $E_{beam} = 60$ GeV.

Figure 11 shows the E_{rec} spectrum for 80 GeV/ c electrons, together with GEANT4 simulations.

The relative difference between the average reconstructed energy $\langle E_{rec} \rangle$ and the beam energy E_{beam} is, to first order, a measure for the signal linearity. Figure 12 shows this quantity as function of E_{beam} , with E_{rec} using all cells in FCal1. In addition, this figure also shows the deviation from linearity when a (symmetric) cell noise cut is applied, i.e. only cells with signals $|E_{rec,i}| > v \cdot \sigma_{noise,i}$

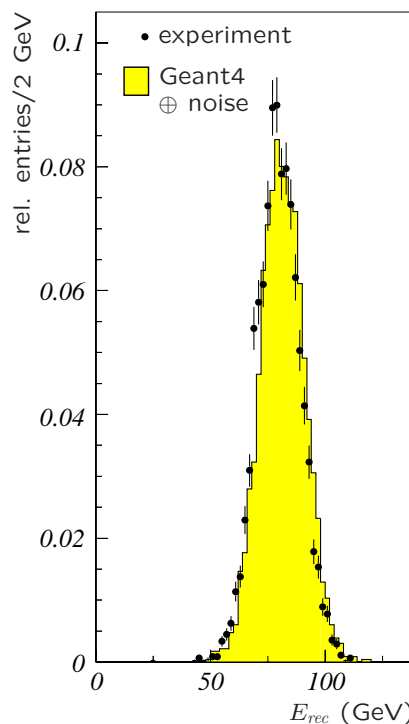


Figure 11. Reconstructed energy (E_{rec}) spectrum for 80 GeV/ c test beam electrons and the corresponding simulations.

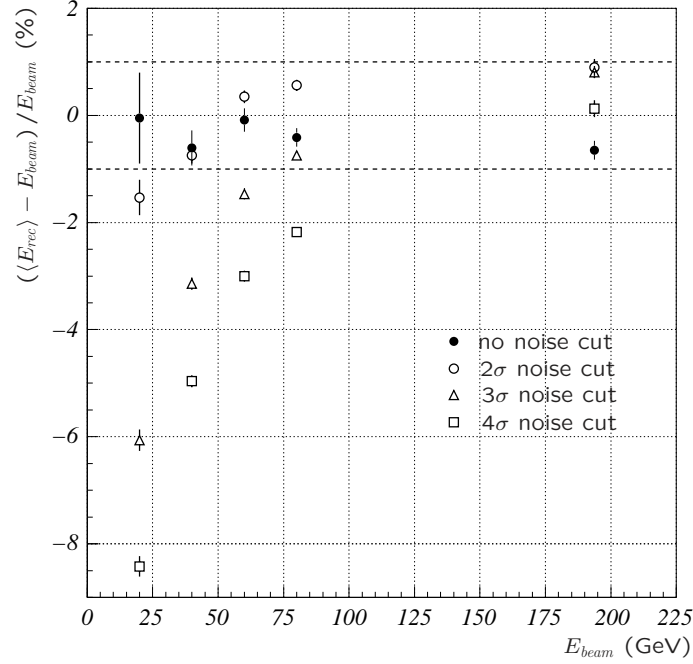


Figure 12. The ratio of average reconstructed electron energy $\langle E_{rec} \rangle$ (see eq. (5.1)) to the beam energy E_{beam} , with and without cell selection with noise cuts (see text), is shown as function of E_{beam} .

enter into the sum in eq. (5.1). Here $\sigma_{noise,i}$ is the energy equivalent of the electronic noise in cell i , as determined by the RMS of the pedestal fluctuations in randomly triggered empty events, and ν sets the noise cut level (typically $\nu \geq 0$).

Clearly there is a strong dependence of the signal linearity on the noise cut level ν . This is expected as the cell selection using any noise cut tends to suppress small true particle cell signals as well, reflected by a more severe relative energy loss, especially at lower energies. The signal gain for $E_{beam} > 40$ GeV and $\nu \geq 2$ is actually generated by the increasing suppression of small negative cell signals around the shower core, which reduce the overall E_{rec} in unrestricted cell energy sums (see further discussion in section 5.3).

The dependence of the reconstructed energy on ν was compared to simulations by calculating the relative difference between the average reconstructed energies from experiment ($\langle E_{rec,exp} \rangle$) and simulations ($\langle E_{rec,sim} \rangle$), with experimental noise included in $E_{rec,sim}$ following the prescription in eq. (4.1) in section 4.3, for various noise cut levels ν like

$$\Delta E / E = \frac{\langle E_{rec,sim} \rangle(\nu) - \langle E_{rec,exp} \rangle(\nu)}{\langle E_{rec,exp} \rangle(\nu)}. \quad (5.2)$$

The dependence of $\Delta E / E$ on ν is shown in figure 13. Note that in addition to the effects of the noise cut another small relative signal loss up to about 2% can be expected at lower energies from the upstream energy losses, see figure 4 in section 2.1. The corresponding variation of $\langle E_{rec,exp} \rangle$, like the signal loss due to the noise cut, was reproduced by GEANT4 in $\langle E_{rec,sim} \rangle$ to order $\pm 2\%$, and slightly worse by GEANT3 (order $\pm 3\%$).

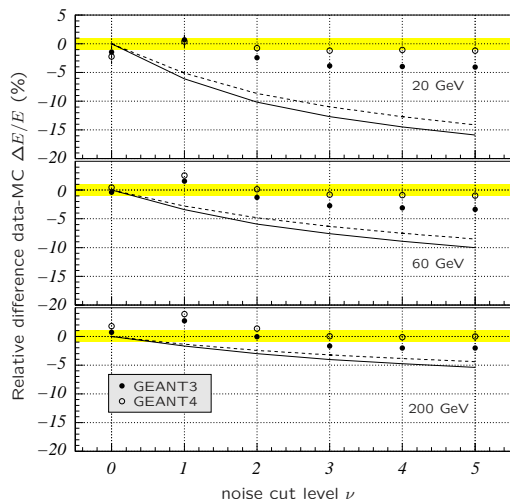


Figure 13. The relative difference of experimental and simulated average energy signals reconstructed with various noise cut levels, for 20, 60 and (nominal) 200 GeV/c electrons in FCal1. The lines indicate the relative loss of electron signal due to the noise cuts, as determined with GEANT3 (solid) and GEANT4 (dashed) simulation.

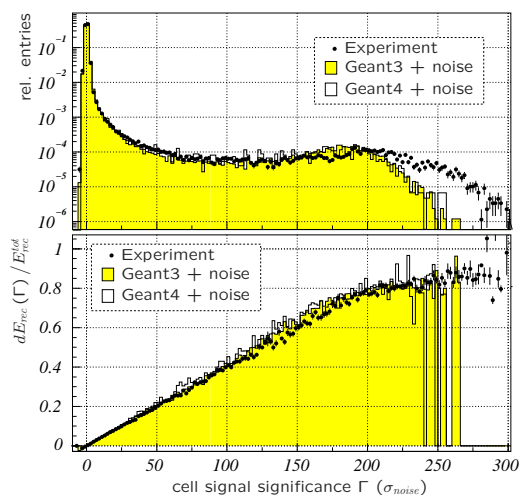


Figure 14. The distribution of the cell signal significance Γ , as defined in the text, for 60 GeV/c electrons in FCal1 (top). The figure at the bottom shows the average relative signal contribution of cells with a given Γ to the total signal for the same events.

The best agreement between simulations and experiment was achieved for the unbiased signal with $\nu = 0$. The effect of the noise cut on the total signal in the simulation depends on the predictive power of the electromagnetic shower model, especially on details of the radial shower development. Another important effect to be considered was to which level the empty events actually describe the electronic noise underlying particle events, especially with respect to coherent fluctuations.

The sensitivity to details of the shower simulation is also indicated in figure 14, which shows the distribution of cell signals in 60 GeV/c electron events, measured in terms of their significance $\Gamma = E_{rec,i} / \sigma_{noise,i}$, for experiment and simulations. The higher end point of the experimental spectrum means that larger signals in a single cell occurred more often in the experiment than in the simulations, thus indicating more compact electromagnetic showers in the experiment.

5.2 FCal1 electron energy resolution

The relative energy resolution is given by $\sigma(E_{rec}) / \langle E_{rec} \rangle$, where both the width $\sigma(E_{rec})$ and the average response $\langle E_{rec} \rangle$ were determined by an unrestricted Gaussian fit to the reconstructed energy (E_{rec}) distributions for various beam energies.

If E_{rec} was calculated according to eq. (5.1) in the previous section, i.e. by summing all FCal1 cell signals for each event, it included a rather large amount of pure electronic noise — the significant part of the electron signal was typically found in one to four cells only, depending on the impact point. Still, by adding the noise to the simulations as prescribed in eq. (4.1) in section 4.3, it was possible to describe the experimental fluctuations quite well with both GEANT3 and GEANT4, see figure 15. This holds even when the noise cut discussed in the previous section was introduced. It

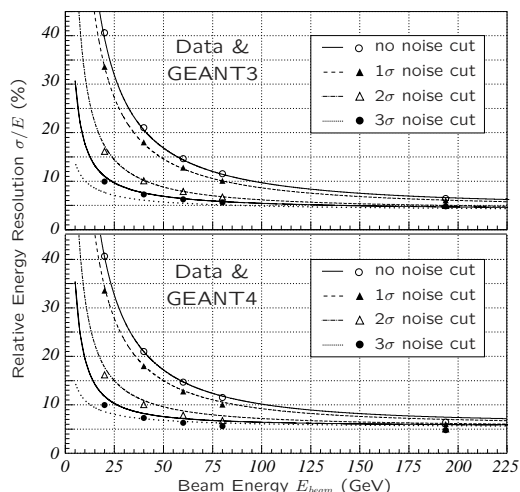


Figure 15. The relative energy resolution for electrons in FCal1, for various noise cut levels ν . The lines are resolution functions determined from simulations. The dotted line shows the intrinsic limit for the resolution, again as determined from simulations.

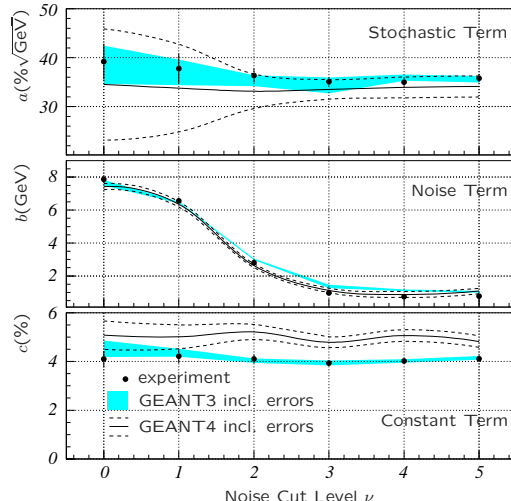


Figure 16. The evolution of the resolution function parameters as function of ν . The shaded areas indicate the parameter error band around their central values for GEANT3, while the solid line shows the central values for GEANT4, with the dashed line indicating the error for this data.

is notable that the fluctuations predicted by GEANT4 simulations at the highest available electron energy (193.1 GeV) are actually larger than in the experiment. The resolution function fitting the beam energy dependence of the relative energy resolution is best given by (see [20], for example)

$$\frac{\sigma(E_{rec})}{E_{rec}} = \sqrt{\left(\frac{a}{\sqrt{E_{beam}}}\right)^2 + \left(\frac{b}{E_{beam}}\right)^2 + c^2}, \quad (5.3)$$

where a measures the stochastic contribution from sampling and intrinsic fluctuations, and b is determined by fluctuations introduced by electronic noise. The variable c is the constant term mostly generated by the already discussed signal fluctuations due to event-by-event variations of the electron impact point, and, for FCal1 to a lesser extent, by channel-to-channel inter-calibration inefficiencies like electronic gain fluctuations.

The dependence of a , b , and c on the noise cut level ν is shown in figure 16. As expected, the stochastic and constant term a and c , respectively, were virtually unaffected by the particular choice of ν . The small ν dependency of these two terms was likely introduced by residual correlations in the numerical fitting of the parameters according to the model given in eq. (5.3). The noise term b drops with increasing ν , again as expected.

Figure 16 also shows that both GEANT3 and GEANT4 described the sampling and intrinsic fluctuations quite well. GEANT4 seems to have larger fluctuations at high energies, as indicated by a larger constant term c . As the noise is introduced into the simulations by overlaying experimental empty events, it is expected that the resolution term b is very similar to the one in the experiment in both GEANT3 and GEANT4.

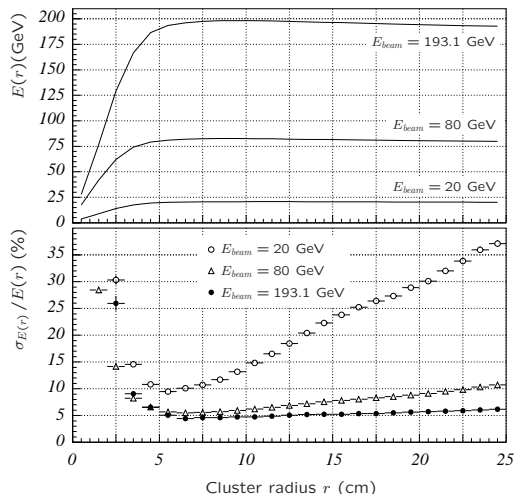


Figure 17. Integrated radial shower profiles for experimental electrons of different beam energies in the FCal1 pre-production prototype (top). The plot at the bottom shows the relative energy resolution $\sigma_{E(r)}/E(r)$ as function of the cluster radius r , for various beam energies E_{beam} .

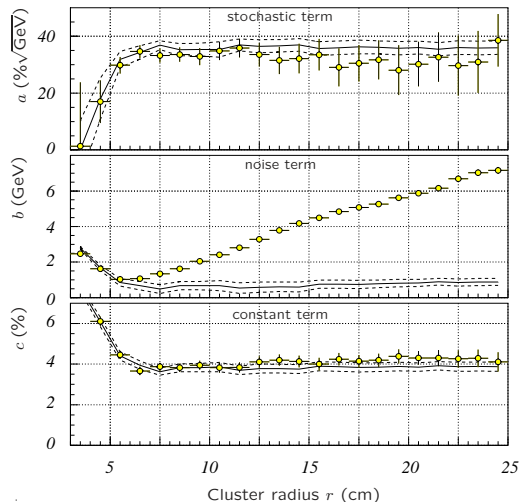


Figure 18. The three parameters of the energy resolution function as function of the cluster radius r . The solid line in these plots mark the central values of the respective parameters if an additional $v = 3$ noise cut is applied on top of the clustering, while the dashed lines indicate the corresponding error bands.

5.3 Cylindrical clustering

Suppression of the electronic noise contribution to the electron signal in FCal1 can be achieved by selecting cells according to their signal significance, as discussed above. Alternatively, the signal collection can be geometrically restricted to the volume in which the electromagnetic shower actually develops. The most appropriate shape for this volume in FCal1 is a cylinder around the direction of flight of the incoming electron, which also defines the principal (longitudinal) shower axis.

The advantage of collecting the signal in cylindrical clusters is that the loss of true signal due to cell selection is avoided. In addition, the radius of the cylinder given the best signal linearity and the best resolution can easily be found experimentally, as indicated in figure 17.

One of the problems with cylindrical clustering is that additional signal fluctuations can be introduced due to the readout granularity. In cell selections only based on the distance between geometrical cell center and shower axis a small shift of the impact point from one event to the next can exclude a cell with significant signal, thus introducing additional impact point dependent signal fluctuations. To avoid this effect, a fraction w of the cell signal contributing to the cluster signal was determined according to the following rule:

$$w = \begin{cases} 1 & \dots\dots\dots \text{ for cells completely inside the cylinder;} \\ \sqrt{\mathcal{A}_{shared} / \mathcal{A}_{cell}} & \text{ for cells partly inside the cylinder;} \\ 0 & \dots\dots\dots \text{ for cells completely outside of the cylinder.} \end{cases} \quad (5.4)$$

Here \mathcal{A}_{shared} is the area of the cell covered by the cylinder on the front face of FCal1, with $0 \leq \mathcal{A}_{shared} / \mathcal{A}_{cell} \leq 1$, and \mathcal{A}_{cell} is the total cell area. The small tilt of the FCal1 module was ignored

in this model; the principal axis of the cylinder (the shower axis) was assumed to be perpendicular to the front face. This introduces the need for a slightly larger cluster radius than the one expected for a tilted principal axis, due to the imposed circular cluster shape instead of the more appropriate ellipsoidal shape. The specific functional choice for w in eq. (5.4) was motivated by aspects of lateral electromagnetic shower development and optimized energy resolution.

Figure 17 shows the integrated radial profiles for electrons in FCal1, as measured by the energy $E(r)$ in a cylinder of radius r . $E(r)$ is at a maximum for $r_{max} \approx 8$ cm, with a small dependence on the electron energy E_{beam} (slightly smaller cylinder preferred for smaller E_{beam}). The fact that $E(r = \infty) < E(r_{max})$ indicates negative signals around the electromagnetic shower generated by differential signal crosstalk in the electronic chain of about 3%, practically independent of E_{beam} (see [12] for details).

The relative energy resolution is also nearly optimal for about the same r_{max} . Increasing r beyond this radius clearly leads to a pick-up of fluctuations due to electronic noise, as can also be seen in figure 17. Again, the result suggests a slightly smaller radius at lower than higher energies. The change of slope at around $r = 15$ cm in the resolution, best seen for $E_{beam} = 20$ GeV, is due to the limited lateral size of the FCal1 module. At this radius the outer radius of the module was reached for some directions from the impact point, while in others cells were still picked up (see figure 5 in section 2.2).

Fitting the parameters of the resolution function in eq. (5.3) for signals in cylindrical clusters of various radii r yields the dependencies on r shown in figure 18. Reasonably accurate determination of these parameters was only possible for $r \geq 4$ cm, as smaller clusters did not collect a sufficient fraction of the electromagnetic shower. The best cluster size deduced from these curves was again about 8 cm. Beyond that only signal fluctuations due to electronic noise were added. The fact that the stochastic resolution parameter a and the constant term c were basically independent of r for $r \geq 6$ cm and only the noise parameter b increased with r , as expected, indicates that the function in eq. (5.3) describes the relative energy resolution for electrons in FCal1 very well, as all parameters were decoupled to a large extent.

An additional cell selection with a noise level $\nu = 3$, as discussed in the previous sections, avoided the noise pick-up at larger radius, as can also be seen in figure 18. Yet, the cylindrical cluster with $r \approx 8$ cm performed as well as the cell noise cut for the resolution, but avoids the signal non-linearities introduced by this particular cell selection, as shown in figure 12 in section 5.1.

Figure 19 shows the domains in the (r, E_{beam}) and the (ν, E_{beam}) plane, respectively, where certain terms in the resolution function eq. (5.3) dominate. Note that for the operation of the FCal1 in ATLAS only the larger E_{beam} regions are relevant, thus the control of the constant term is most important for a good electron reconstruction performance.

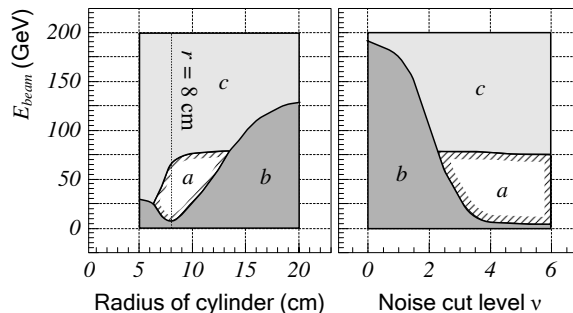


Figure 19. The domains in (r, E_{beam}) and (ν, E_{beam}) in which given terms a , b , and c of the resolution function dominate.

	Resolution Fits		σ/E (193.1 GeV)
	a ($\% \cdot \sqrt{\text{GeV}}$)	c (%)	(%)
impact point corrected	33.51 ± 0.71	2.35 ± 0.16	3.43 ± 0.15
cylindrical cluster ($r = 7$ cm)	34.60 ± 2.24	3.66 ± 0.21	4.43 ± 0.11

Table 1. Energy resolution contributions for electron signals in FCal1, corrected for impact point fluctuations or collected in a cylindrical cluster. In addition the resolution at the highest available E_{beam} is given.

5.4 Further optimization of the energy resolution

The inhomogeneous FCal1 front face suggests explicit corrections of the signal depending on the impact point. This impact point was rather well known for each particle from its reconstructed track (typically within ± 0.5 mm or better in each dimension). Table 1 summarizes the most important electron energy resolution parameters in case of cylindrical clustering and when an explicit impact point correction based on the reconstructed track is applied in addition. The latter indicates the best possible performance of FCal1 for electrons. As reconstructed tracks are not going to be available for the FCal in ATLAS, an alternative approach to impact point reconstruction using only FCal signals was developed and is discussed in the following section.

5.5 Impact point reconstruction

The lack of a tracking device in front of the FCal in ATLAS lead to the development of an impact point reconstruction algorithm using FCal signals alone. A straight forward approach using the signal center of gravity only was first explored. It allowed a coarse reconstruction of the impact point, as illustrated in figure 20. The rather large lateral cell size in FCal1, especially with respect to the lateral extension of electromagnetic showers in this calorimeter, meant that for many electrons a large fraction of the signal was contained in one cell only, thus pulling the reconstructed center of gravity towards the geometrical centers of this cell, see figure 20(a)-(c). A more careful analysis actually showed that even electrons with a very large fraction of their signal in only one cell had their shower center of gravity slightly off the geometrical cell center, due to the small but finite incident angle.

The energy sharing between cells generating the particular center of gravity distribution is shown in figure 20(d) and (e). Center of gravities were reconstructed close to the geometrical cell center, as discussed above, in showers where typically 80 to 90% of the electron energy was deposited in one cell alone. A center of gravity between two cells, on the other hand, implies equal sharing of energy between the two cells alone.

A more evolved method for impact point reconstruction explored details of the spatial signal pattern generated by the lateral electromagnetic shower spread in the FCal1 cells, and its relation to the impact point. This method consisted of two steps. At first, the pattern was established in look-up tables using 193.1 GeV/c electrons. The sensitive variable used was the energy sharing between any two cells, given by

$$F_{ij} = \frac{E_i - E_j}{E_i + E_j}. \quad (5.5)$$

It was calculated for pairs of cells ($i, j, i \neq j$) with significant signals E_i, E_j in the reference events, and then binned in steps of typically 0.2 for $-1 \leq F_{ij} \leq 1$.

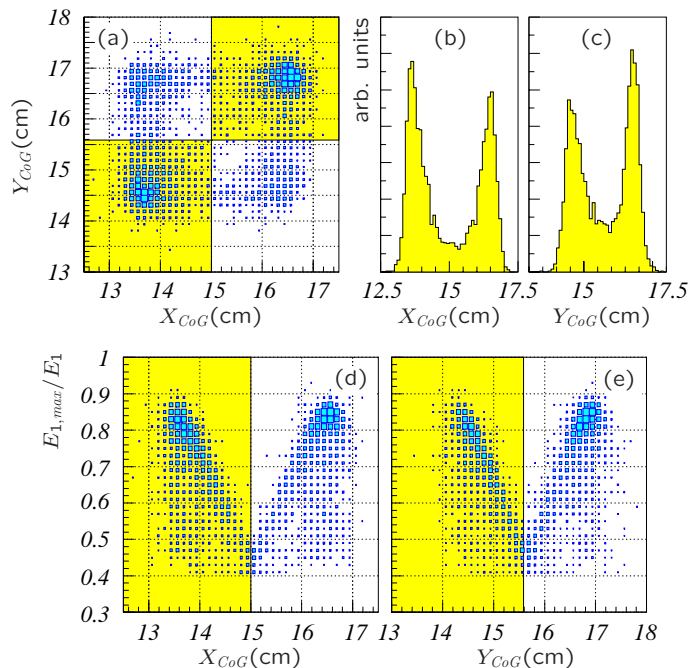


Figure 20. The distribution of the center of gravities for 80 GeV/ c electrons on the front face of the FCal1 pre-production prototype (a). The shaded and open boxes indicate cells. The distributions of the horizontal (X_{CoG}) and vertical (Y_{CoG}) center of gravity coordinates are shown in (b) and (c), respectively. The graphs on the bottom show the ratios of the maximum cell signal $E_{1,max}$ over the total signal E_1 in FCal1 as function of X_{CoG} (d) and Y_{CoG} (e).

The other feature used to classify the pattern was the geometrical (neighbouring) relation between the two cells in a given pair. These relations were categorized as common edge left/right or up/down,⁷ common corner points (top, left)/(top, right), (bottom, left)/(bottom, right), separated by one or two cell(s) (left, right, top, bottom, or along a diagonal), and others.

The impact point coordinates from the tracking system were then stored for each F_{ij} bin, and each geometrical cell relation, producing patterns as shown in figure 21. Similar patterns of many reference events are overlaid to calculate the probability contours for the impact point. Finally, the combined probability for all geometrical relations and F_{ij} bins was calculated by adding the logarithms of the individual probabilities.

In the second (reconstruction) step the pattern characteristics of any given electron event were calculated in the same space of F_{ij} bins and geometrical relationships. The most likely impact point was then looked up in the probability contours for the found pattern, as determined with the 193.1 GeV/ c electron data. No significant energy dependence of the patterns was expected, at least not at a level significant for the impact point reconstruction, as the lateral shower profiles show only a very slight energy dependence themselves.

Obviously this method made optimal use of the cell segmentation in FCal1, and was certainly found to be much less sensitive to the relation between lateral cell and shower size than the center of gravity approach. Using the impact point reconstructed with this approach allowed a realistic

⁷The cells are actually rectangles, i.e. left/right is different from top/bottom.

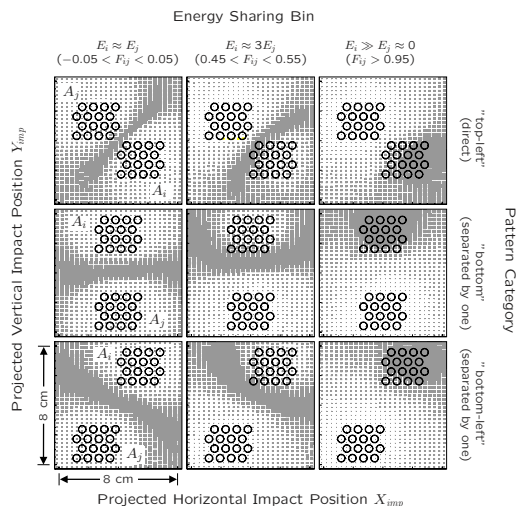


Figure 21. Distributions of impact points on the FCal1 front face for three different bins of the signal sharing variable F_{ij} (see text) and three different geometrical relations between the paired cells A_i, A_j . Each cell is indicated by a group of 16 electrodes.

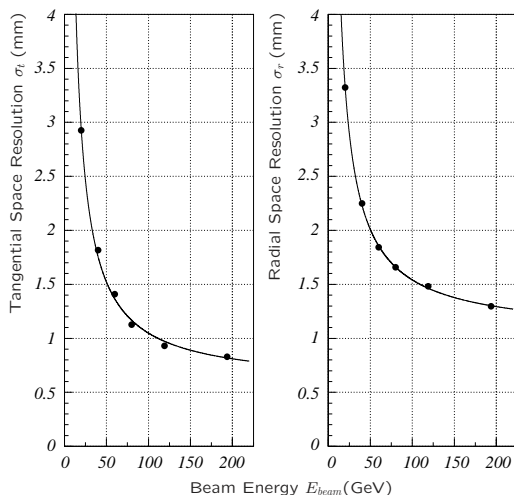


Figure 22. The tangential (σ_t) and radial (σ_r) space resolution for electrons in FCal1, as function of the beam energy E_{beam} . The curves show results from fits to the data points as described in the text.

measurement of the spatial resolution for electrons in the FCal. Figure 22 shows the radial and azimuthal (tangential) space resolution as function of the beam energy. The energy dependence of the spatial resolution functions could be described by

$$\sigma_s = \sqrt{\left(\frac{a_s}{\sqrt{E_{beam}}}\right)^2 + \left(\frac{b_s}{E_{beam}}\right)^2 + c_s^2}. \quad (5.6)$$

The interpretation of the parameters a_s , b_s , and c_s corresponds to the interpretation of the energy resolution function given in eq. (5.3) in section 5.2, with $s = t$ for the tangential and $s = r$ for the radial resolution. Table 2 summarizes the results from the determination of these parameters.

Extrapolating these results to single electrons in the FCal1 in ATLAS yields a high energy limit in the resolution of the pseudo-rapidity measurement $\sigma_\eta \approx 0.009$ at $|\eta| = 3.7$, well below

	a_s (mm · $\sqrt{\text{GeV}}$)	b_s (mm · GeV)	c_s (mm)
tangential ($s = t$)	10.58 ± 0.23	42.0 ± 1.4	1.10 ± 0.02
radial ($s = r$)	8.02 ± 0.16	46.9 ± 0.8	0.57 ± 0.02

Table 2. The stochastic (a_s), noise (b_s) and constant term (c_s) of the electron space resolution in FCal1, as determined by fits of the resolution function in eq. (5.6) to the experimental data shown in figure 22.

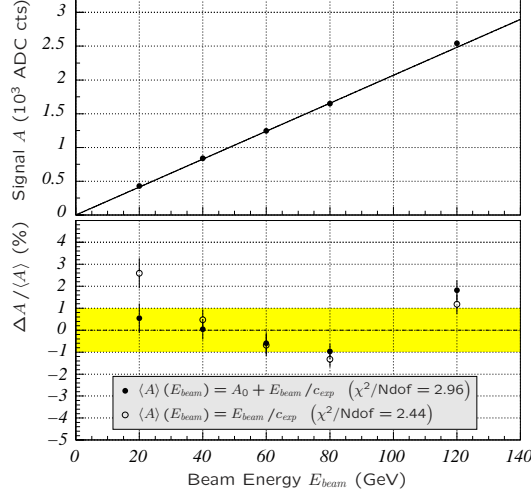


Figure 23. The average experimental electron signal in FCal2 as a function of the beam energy E_{beam} , and its deviation from the fitted line for two different fit models, see eq. (6.1).

the ATLAS requirement of $\sigma_\eta < 0.05$ discussed in the introduction section 1. The test beam result excludes possible additional resolution loss due to longitudinal vertex fluctuations. The uncertainty in azimuth at the same pseudo-rapidity η is $\sigma_\phi \approx 2.4$ mrad.

The application of the impact point likelihood patterns is under study for best possible direction reconstruction in the ATLAS FCal. It is particularly interesting for the highly focussed, therefore narrow in linear space, particle jets going in the forward direction at LHC, as for those the electromagnetic and hadronic showers sizes in the FCal will actually be larger than the typical sizes of the jets themselves. This may allow using the same likelihood patterns derived from electron test beam signals in FCal1, with some loss of resolution due to the fact that the incoming energy will already be distributed in space in the (small) jet cone, and that some of the hadronic shower activity in FCal1 will introduce additional fluctuations in F_{ij} and thus in the reconstructed patterns as well.

6. The electron response in FCal2

The electron response of the hadronic FCal2 module is an important performance parameter for the determination of the energy scale for this module. On the other hand, the design of FCal2 was optimized for reconstructing hadron jets in an environment characterized by large signal fluctuations introduced by a high rate of soft collisions underlying the hard scattering events at LHC. One important requirement for a calorimeter operating in this environment is to keep the spatial hadronic shower extent as small as possible, thus requiring a very dense detector. The price to pay then is loss of performance especially for electromagnetic energy due to the small sampling

fraction. Less than 1% of the energy in an electromagnetic shower in FCal2 is actually converted into signal. The dense tungsten absorber also limits the shower sizes such that an analysis of topological features, similar to what has been presented for FCal1 in the previous section, was difficult. The total electromagnetic shower depth is only about 15 cm, i.e. one third of the total FCal2 depth, and the Moliere Radius R_M is about 11.5 mm. The relatively large lateral cell sizes in FCal2 thus often confine the electron signal to one channel. Nevertheless, it was possible to extract the basic electromagnetic calibration constant, as discussed in the following paragraphs.

6.1 Electron signal linearity in FCal2

The dependence of the average FCal2 electron signal $\langle A \rangle$ on the beam energy E_{beam} is shown in figure 23. It shows a linear response at the level of $\pm 2\%$, depending on the definition of the proportionality between $\langle A \rangle$ and E_{beam} . Two cases have been studied with this respect, first with a linear model assuming only one constant proportionality factor $c_{exp,a}$, and second with $c_{exp,b}$ and an additional signal offset A_0 , so that

$$\begin{aligned} \langle A \rangle (E_{beam}) &= E_{beam} / c_{exp,a} \quad \text{or} \\ \langle A \rangle (E_{beam}) &= A_0 + E_{beam} / c_{exp,b} . \end{aligned} \quad (6.1)$$

For this analysis the average $c_{exp} = (c_{exp,a} + c_{exp,b}) / 2$ is considered the electromagnetic calibration constant (in units of GeV/ADC cts) in FCal2. The small difference between $c_{exp,a}$ and $c_{exp,b}$ is absorbed into the systematic error of c_{exp} .

Comparing c_{exp} for FCal2 with the corresponding number for FCal1 yields the ratio of electron calibration constants R_c between the two modules to be

$$R_c = \frac{c_{exp}(\text{FCal2})}{c_{exp}(\text{FCal1})} = 1.852 \pm 0.041(\text{sys.}) \pm 0.022(\text{stat.}) .$$

The ratio of sampling fractions R_s can be extracted from this experimental result by applying a correction for the different pulse shapes in FCal1 and FCal2:

$$R_s \approx \frac{R_c}{1.3} = 1.425 .$$

The magnitude of this correction was determined by an analysis of the signal shape evolution using a detailed PSpice⁸ simulation of the involved electronic circuits and transmission lines, including a model of the electric properties of the FCal electrodes.

R_c and R_s are important parameters for the reconstruction of hadronic showers in FCal1 and FCal2, where the energy sharing, as measured by the electromagnetic energy scale signals in the modules, may enter into the calibration functions.

6.2 Signal impact point dependence

The strong impact point dependence of the signal, already discussed earlier and observed even for the slightly tilted FCal2 module, was an indication of the fact that the energy sampled in the active liquid argon gap of the electrodes was severely reduced when the electron hit the electrode rod first, for example, due to the very dense tungsten. This can be seen in figure 24, where the electron signal is shown as function of the distance between the particle impact point and the center of the electrode rod.

⁸Registered trademark of Cadence Design Systems, Inc.

The signal shape displayed in this figure can be directly mapped onto the electrode geometry. There is a deep minimum, corresponding to a relative signal loss of more than 30%, in the center of the electrode rod. Here the electrons hit pure tungsten first.

Going outward, it is followed by a signal maximum at the (expected) location of the liquid argon gap. The next signal minimum can then be found further out at the location expected from the hexagonal electrode pattern, roughly between two to three liquid argon gaps. It is less pronounced because at this location the electrons actually hit the FCal2 copper end plate first, which represented a target of relatively soft material. It therefore generated secondaries with longer range, thus distributing the incoming electron energy in space and increasing the likelihood for these secondaries to actually reach the sensitive liquid argon.

The impact point dependence of the electron signal in FCal1 was less severe, especially when the module was slightly tilted with respect to the beam axis. At 0° impact angle, a variation of only 10% or less was observed [8]. This was mainly due to the fact that the softer copper allows a much larger longitudinal and radial shower expansion which significantly increases the amount of active argon passed by the shower particles, compared to the denser tungsten in FCal2. More specifically, the longitudinal coupling due to the nearly threefold increase of the longitudinal shower size, together with a larger Moliere Radius in FCal1 ($R_M \approx 16$ mm, compared to about 11.5 mm in FCal2), involves many more electrodes in the signal formation, thus increasing the sampling fraction significantly.

7. Conclusions and outlook

Results from a detailed study of the electron response of the ATLAS Forward Calorimeter, using both experimental data from the 1998 pre-production prototype test beam and simulations within the GEANT3 and GEANT4 frameworks, have been presented. Important performance parameters like signal linearity for electron energies from 20 to about 200 GeV, and the energy resolution in the same energy range, were found to be well within the requirements for ATLAS physics for the electromagnetic FCal1 module: deviations from linearity were within $\pm 1\%$, and the most important high energy limit in the energy resolution was of order 4%.

The 1998 test beam offered the unique chance to directly access the electromagnetic response of the hadronic FCal2 module experimentally. The module showed the expected direct proportionality between signal and incoming electron energy, thus confirming that the electromagnetic energy scale signal in FCal2 is a good base for energy reconstruction for hadrons and jets. This

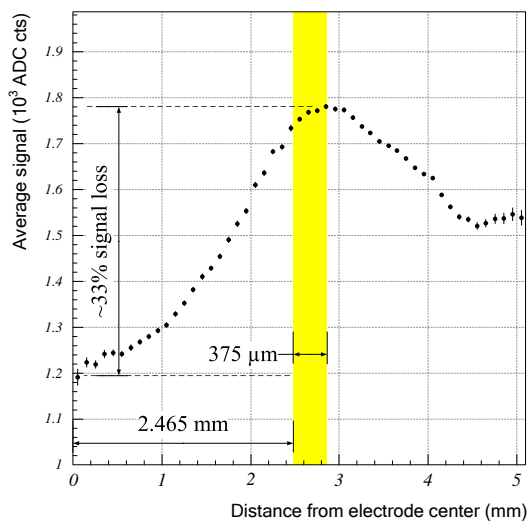


Figure 24. The variation of the signal of 80 GeV/c electrons in the experiment as function of the distance between the electrode center and the particle impact point. The electrode structure is clearly reflected in this response.

conclusion was non-trivial due to the very small sampling fraction and other particular signal features like a very strong impact point dependence, introduced by the dense absorber and the tubular readout geometry.

Direct comparisons of the experimental data with the two different simulations indicated that the average electron signal in FCal1 in the available energy range can be understood at the level of one percent. Some significant differences were found, though, in some details of the shower development. The electromagnetic showers in the experiment seemed to be more compact (narrower) with higher cell signal densities than the ones modeled in GEANT3 and GEANT4. This observation has not yet been confirmed with more modern GEANT4 versions like GEANT4.8.2 and newer, which feature (among others) significant improvements of the modeling of multiple scattering in electromagnetic showers. A more decisive conclusion on this issue has to be left to more recent studies, probably with data from the 2003 ATLAS FCal test beam experiment. Here it is notable that GEANT3 and GEANT4 at the state of art of this analysis agree quite well with each other.

Meanwhile, the production modules for FCal1, FCal2, and FCal3 have been built (two of each). A full FCal calorimeter was subjected to extensive test beam studies with electrons, pions, and muons in summer of 2003, and the pre-production prototypes for FCal1 and FCal2 used in the test beam described in this article were rebuilt for another specific test beam experiment illuminating the transition region between the ATLAS end-cap and forward calorimeters around $\eta = 3.2$ with all three particle types in 2004.

Acknowledgments

We are very grateful to the ATLAS Liquid Argon and Test Beam communities for their help with the FCal test beam effort in 1998. In addition, we like to thank M. Donkers, D. Paterson, D. Waller (all Carleton University, Ottawa, Canada, at the time of the data taking), and J. Kamnitzer (University of Toronto, Toronto, Canada, at the time of the data taking) for their contributions. We also like to thank all involved members of the CERN staff for their support, especially N. Doble and K. Elsener for providing excellent beams for this experiment. P. Gumplinger (TRIUMF, Vancouver, Canada), J. Apostolakis (CERN), M. Maire (LAPP Annecy, France), and other members of the GEANT4 collaboration and the ATLAS-GEANT4 Comparison Project provided a lot of help with GEANT4, which we thankfully acknowledge. We thank M. Vinciter and L. Heelan (both Carleton University) for their careful reading of the manuscript. Last but not least we like to thank our funding agencies for their continuing support.

A. Module geometry details

The bulk absorber of the FCal1 pre-production prototype consists of 18 copper plates, each 2.5 cm thick, stacked to a total depth of 45 cm, thus forming a basically monolithic copper wedge with a 90° opening angle. The module depth corresponds to about $28 X_0$ and 2.7 absorption lengths (λ).

Each plate has 2351 holes drilled into it in a hexagonal pattern, to accommodate the electrodes, see figure 3 in section 2. The outer radius of the FCal1 wedge is about 45 cm. The total weight of the module is approximately 0.5 t.

Overall Geometry & Materials	FCal1	FCal2
Module outer radius [cm]	45	45
Module depth [cm/ X_0 / λ]	45/27.6/2.7	45/91.2/3.7
Bulk absorber material	Cu	97%W 2%Ni 1%Fe [†]
Tube material	Cu	Cu
Rod material	Cu	W
Approximate module mass [t]	0.5	0.9
Average module density [g/cm ³]	7.9	14.5
Electrode Geometry	FCal1	FCal2
Tube inner diameter [mm]	5.24	5.68
Rod outer diameter [mm]	4.71	4.93
Average liquid argon gap size [μ m]	267	375
Electrode center-to-center distance ... [mm]	7.50	8.18
Calorimetric Parameters	FCal1	FCal2
dE/dx weighted sampling fraction [%]	1.61	1.32
dE/dx weighted sampling frequency [cm ⁻¹]	0.60	0.35
Approx. electron sampling fraction [%]	1.4	1.0
Electronic Parameters	FCal1	FCal2
Electron drift time [ns]	53	75
Potential across gap [V]	250	375
Electrode capacitance [pF]	349	263
Number of electrodes	2351*	2550*
Number of readout cells (tiles)	192	128
Number of readout channels (total/bi-gain) .	256/64	160/32

[†]average slug composition only.

*not all connected.

Table 3. Most important module parameters for the FCal pre-prototypes. The electron sampling fractions have been estimated with GEANT3 and GEANT4 simulations, while the dE/dx weighted sampling fraction and -frequency have been calculated for the corresponding detector geometries.

The FCal2 absorber is built from small tungsten slugs, which fill the interstitial space between the tube electrodes. Two copper end plates hold the electrodes in position and contain the slugs inside the detector volume, together with copper form pieces on the sides and at the inner radius of the module. The overall depth is 45 cm, which due to the much denser absorber corresponds to about 91 X_0 and 3.7 λ . The module weight is about 0.9 t. This module has 2550 individual electrodes in one quarter of the volume of the final detector. Table 3 summarizes the most important mechanical parameters of both modules.

References

- [1] ATLAS collaboration, *ATLAS Detector and Physics Technical Design Report*, CERN/LHCC/99-14/15 (1999).
- [2] ATLAS Liquid Argon collaboration, *Liquid Argon Calorimeter Technical Design Report*, CERN/LHCC/96-41 (1996).
- [3] ATLAS collaboration, *ATLAS Calorimeter Technical Design Report*, CERN/LHCC/96-40 (1996).
- [4] J.P. Rutherford, *Signal degradation due to charge buildup in noble liquid ionization calorimeters*, *Nucl. Instrum. Meth. A* **482** (2002) 156.
- [5] P. Loch, *Proc. VIIIth Int. Conf. on Calorimetry in High Energy Physics, Lisbon, 1999*, G. Barreira, A. Gomes, A. Maio, B. Tome and M.J. Varanda ed., World Scientific, Singapore (2000).
- [6] J. Armitage et al., *Results for electrons from the 1995 ATLAS forward calorimeter prototype testbeam*, Proc. 5th Int. Conf. on Advanced Technology and Particle Physics, Como 1996, E. Borch, S. Majewski, J. Huston, A. Penzo and P.G. Rancoita ed., *Nucl. Phys. B (Proc. Suppl.)* **61** (1998) 101.
- [7] J.P. Rutherford, *The ATLAS Forward Calorimeters*, Proc. VIth Int. Conf. on Calorimetry in High Energy Physics, Frascati 1996, A. Atonelli, S. Bianco, A. Calcutera and F.L. Fabbri ed., *Frascati Physics Series* **6** (1996) 35.
- [8] M.I. Ferguson et al., *Electron testbeam results for the ATLAS liquid argon forward calorimeter prototype*, *Nucl. Instrum. Meth. A* **383** (1996) 399.
- [9] R. Brun and F. Carminati, *GEANT Detector Description and Simulation Tool*, CERN Programming Library Long Writeup W5013 (1993).
- [10] GEANT4 collaboration, S. Agostinelli et al., *GEANT4 — A simulation toolkit* *Nucl. Instrum. Meth. A* **506** (2003) 250.
- [11] P. Loch, *Tube radius optimization for the ATLAS electromagnetic forward calorimeter*, ATLAS Internal Note LARG-NO-39 (1996).
- [12] J.C. Armitage et al., *Electron Results for the ATLAS Electromagnetic Forward Calorimeter Module 0 Test Beam 1998*, ATL-LARG-2003-011 (2002).
- [13] R.L. Chase, C. de la Taille, S. Rescia and N. Seguin-Moreau, *Transmission line connections between detector and front end electronics in liquid argon calorimetry*, *Nucl. Instrum. Meth. A* **330** (1993) 228.
- [14] R.L. Chase, C. de la Taille and N. Seguin-Moreau, *Experimental results on cable-coupled preamplifiers*, *Nucl. Instrum. Meth. A* **343** (1994) 598.
- [15] C. de la Taille, *Automated system for equivalent noise charge measurements from 10 ns to 10 μ s*, Proc. Int. Conf. on Advanced Technology and Particle Physics, Como 1992, *Nucl. Phys. B (Proc. Suppl.)* **32** (1993) 449.
- [16] A. Savine et al., *Position measurements and response uniformity of the LAr FCAL*, Proc. VIIth Int. Conf. on Calorimetry in High Energy Physics, Tucson, 1997, E. Cheu, T. Embry, J. Rutherford and R. Wigmans eds., World Scientific, Singapore (1998).
- [17] A. Savine et al., *Beam test of liquid argon tube calorimeter prototype*, Proc. Vth Int. Conf. on Calorimetry in High Energy Physics, Upton, New York 1994, H.A. Gordon and D. Rueger eds., World Scientific, Singapore (1995).

- [18] H1 Calorimeter Group, B. Andrieu et al., *Beam tests and calibration of the H1 liquid argon calorimeter with electrons*, *Nucl. Instrum. Meth.* **A 350** (1994) 57.
- [19] P. Loch, *Suggestions for a General Energy Reconstruction Scheme for the ATLAS Calorimeters*, ATLAS Internal Note CAL-NO-91 (1997).
- [20] J. Engler, *Status and perspectives of liquid argon calorimeters*, *Nucl. Instrum. Meth.* **A 225** (1984) 525.